Supporting Information

Fast Stiffness Mapping of Cells Using High-Bandwidth Atomic Force Microscopy

Andrew Wang[1], Karthik Vijayraghavan[2], Olav Solgaard[2], and Manish J. Butte[1]

[1] Department of Pediatrics, Stanford University, Stanford, CA

[2] Department of Electrical Engineering, Stanford University, Stanford, CA

Supporting Figures

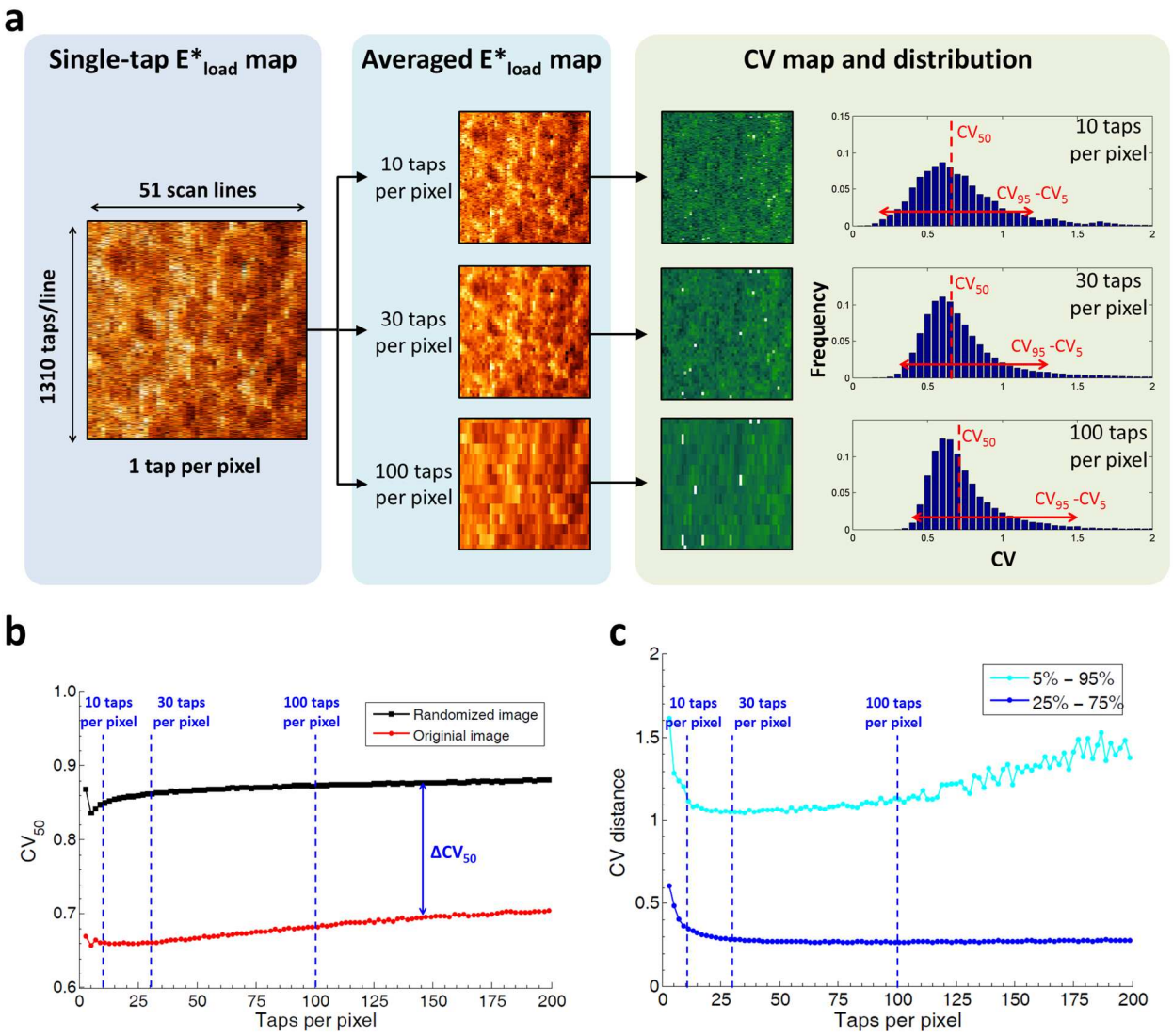

Figure S1. Optimal averaging of the single-tap stiffness map by evaluating the distribution of coefficient of variation (CV) as a function of number of taps per pixel (based on Fig. 3b). a. Calculation of CV distribution. (left) The single-tap stiffness (E^*_{load}) map consists of 1310 taps per scan line and 51 lines. To search for the optimal number of taps per pixel, averaged stiffness maps are calculated using different number of taps per pixel. (middle) For example, the averaged stiffness maps with N=10, 30, or 100 taps per pixels are shown. (right) The corresponding CV maps are then calculated where each pixel in the map is the

epresents its local uncertainty of stiffness measurement. Finally, median CV (CV_{50}) and CV ranges are extracted from the CV distributions. The same procedure is also applied to the permuted or scrambled stiffness map. **b.** CV_{50} of the original image (red curve) is lower than that of the scrambled image (black curve) for any number of taps per pixel. The difference of the two curves (ΔCV_{50}) is shown in Fig. 3a. **c.** The range of 5 to 95 percentile (cyan curve) and interquartile distance (25 to 75 percentile, blue curve) reveal that the distribution of CV is the narrowest around 20-30 taps per pixel.

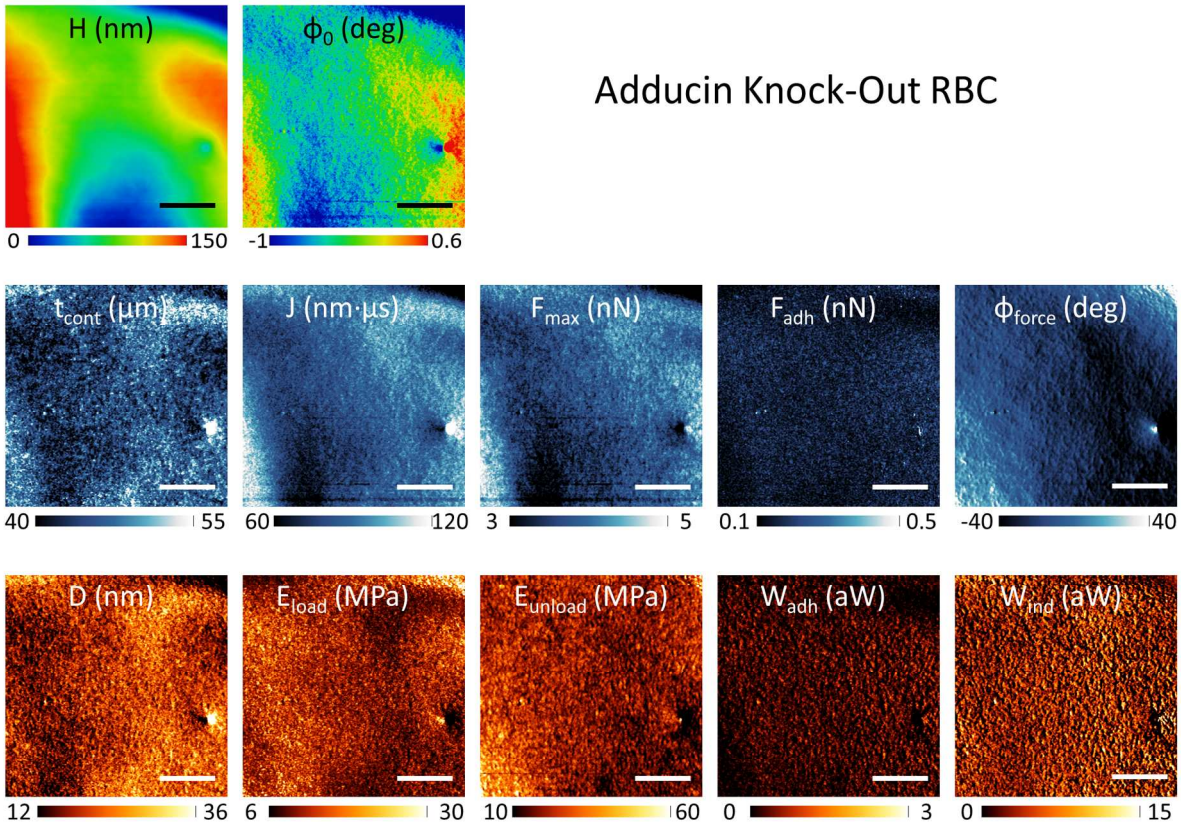

Figure S2. Nanomechanical images of an alpha-adducin knock-out mouse red blood cell (RBC). Top row, Conventional topography (H) and phase (φ_0) images (256×256 pixels) as in tapping-mode AFM. **Middle row,** Images of nanomechanical properties directly measured from the time-resolved tip-sample interaction force. The same notations from Fig. 2 were used here**. Bottom row,** Images of nanomechanical properties derived from reconstructed force-distance curves using calculated indentation. The meshwork observed in wild-type RBCs was absent here. Scale bar is 0.5 μm and image size is 841 × 256 pixels.

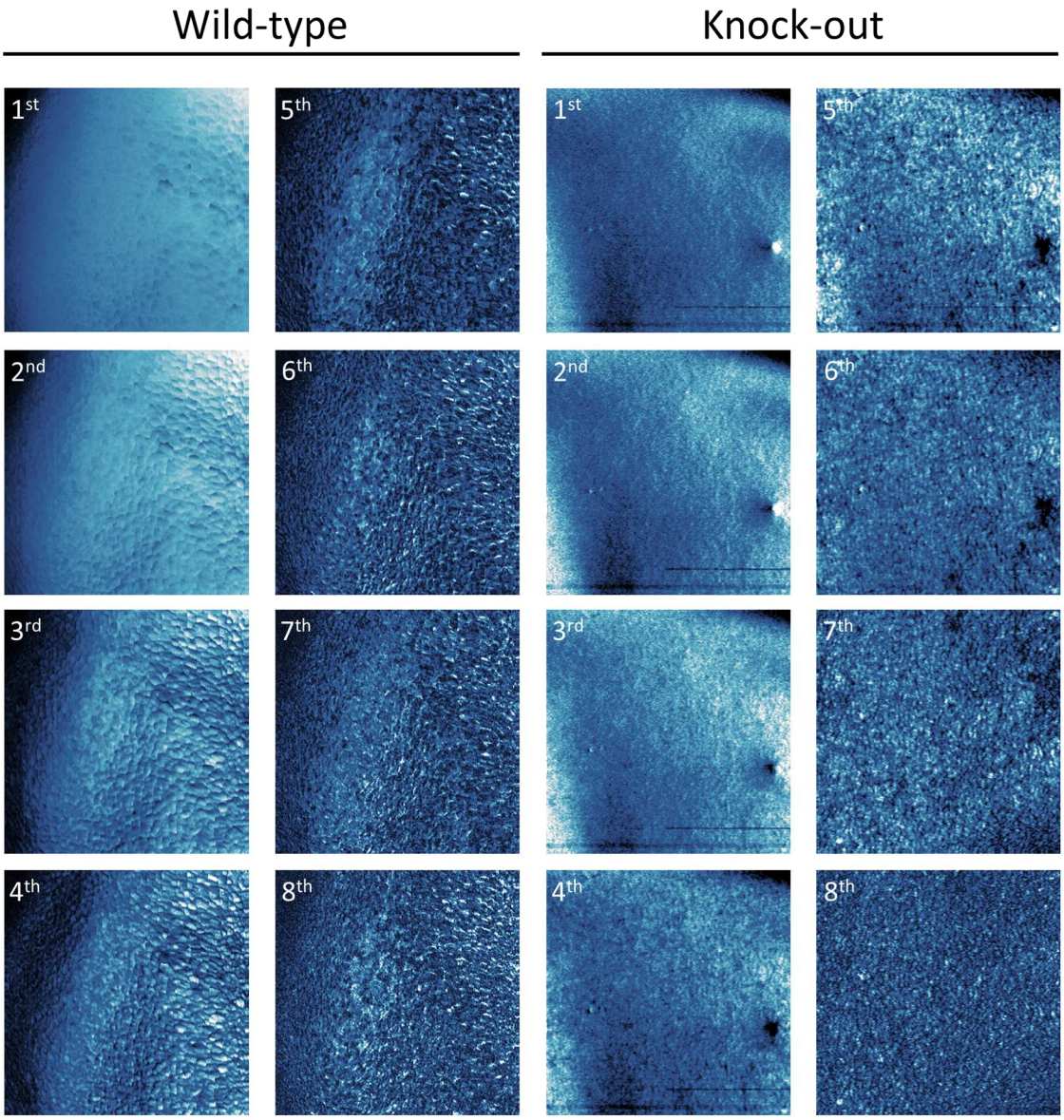

Figure S3. Harmonic images of wild-type and alpha-adducin knock-out mouse RBCs. Root-mean-squared amplitude of harmonics from the 1st to the 8th order were calculated from the force signal using comb filtering. The same regions in Fig. 2 and Fig. S2 are shown here. Each harmonic image shows distinct contrast and seems to be sensitive to different nanomechanical properties.

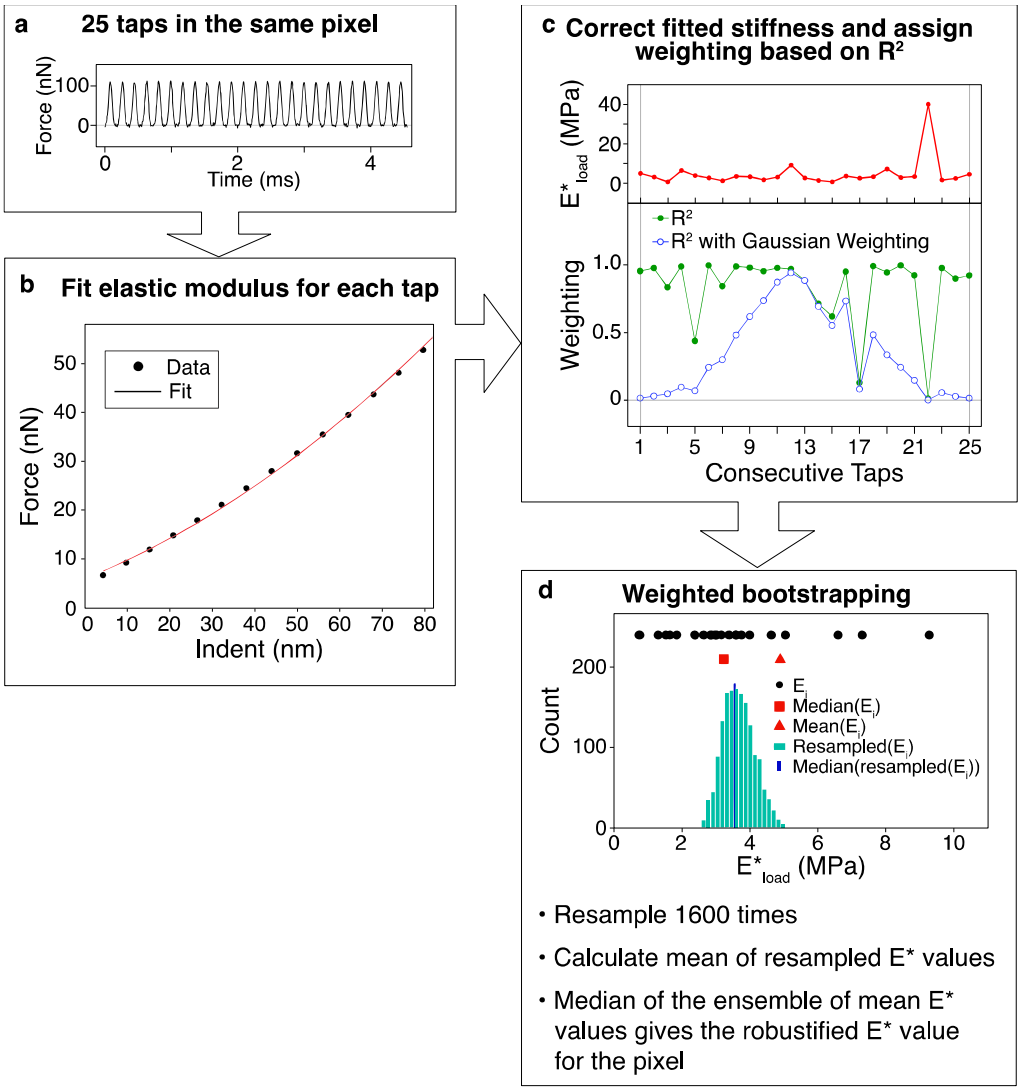

Figure S4. Weighted bootstrapping method. a. The force signal of 25 consecutive taps in the same pixel. **b.** Each tap in the same pixel was fitted to a Hertzian contact mechanical model to extract the elastic modulus (E^*) and the goodness-of fit value (R^2). **c.** Weighting for each tap was calculated based on R^2 and the spatial position of each tap. The clearly aberrant tap #22 here was downweighted because of Gaussian weighting. **d.** Bootstrapping resampling of the 25 E^* values 1600 times using the weightings determined in c. The 25 raw E^* values (black solid circles) are plotted on the top, followed by the median (red solid square) and mean (red solid triangle) of the raw E^* values, and the histogram (green bars) of the mean of resampled E^*. In this example, the median of the resampled E^* distribution (blue line) was higher than the median directly calculated from the raw E^* values.

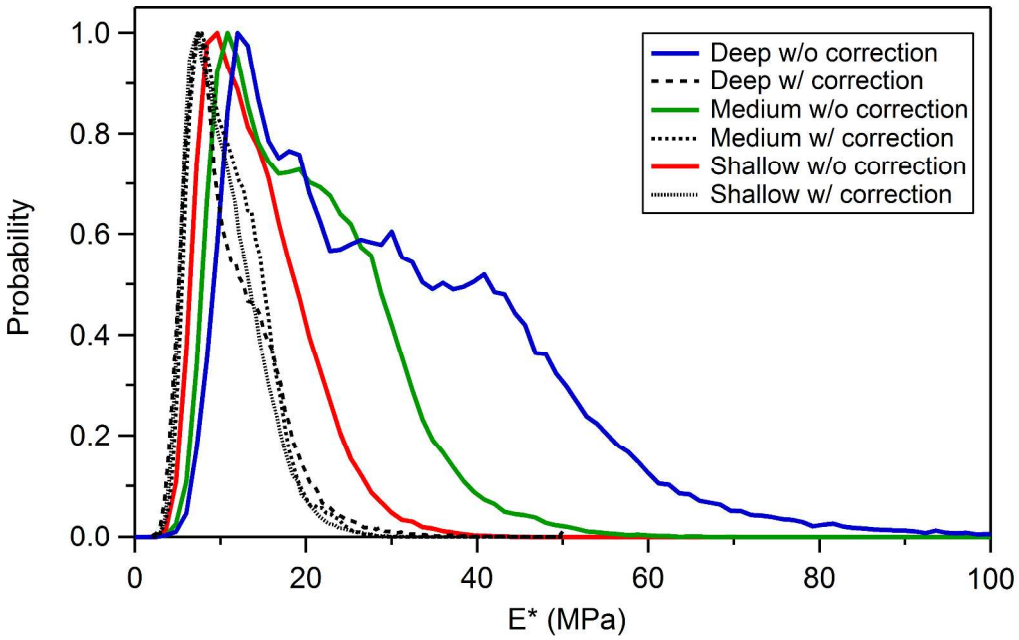

Figure S5. Histogram of stiffness distributions at the three indentation ranges. Thin-film correction removed contribution from the stiff substrate and collapsed the distributions down to the same stiffness range.

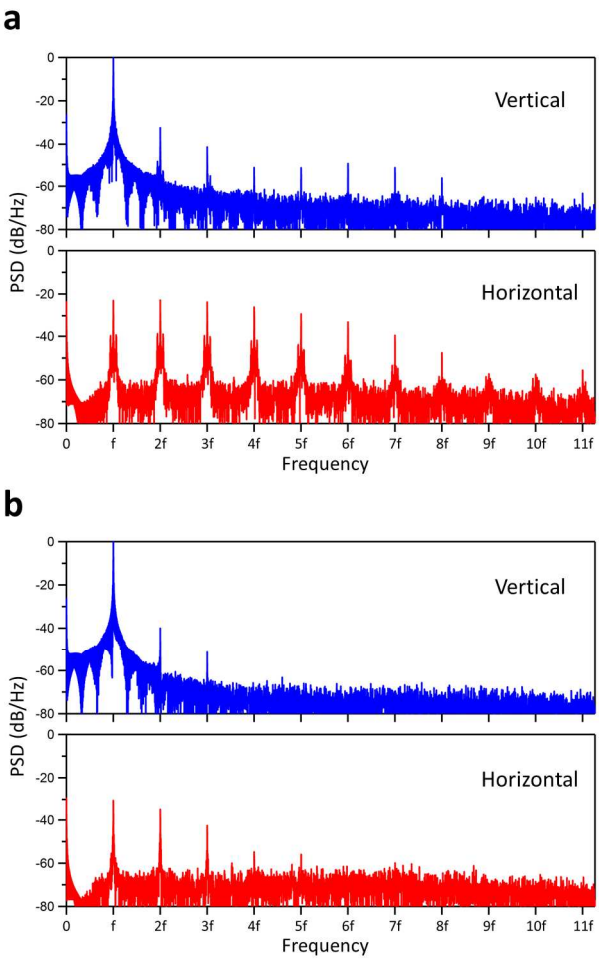

Figure S6. Higher-harmonic contents in the vertical and horizontal signals. a. Frequency spectrum acquired from tapping the glass substrate. Harmonics up to the 8^{th} and 11^{th} order are shown in the vertical and horizontal signals, respectively. **b.** Frequency spectrum acquired from tapping the cell surface. Harmonics up to the 3^{th} and 5^{th} order are observed in the vertical and horizontal signals, respectively. The spectra were calculated from 255 taps (~10 pixels) in the two regions of interest (glass and cell) in Fig. 5. The drive frequency (f) was 5.9 kHz.

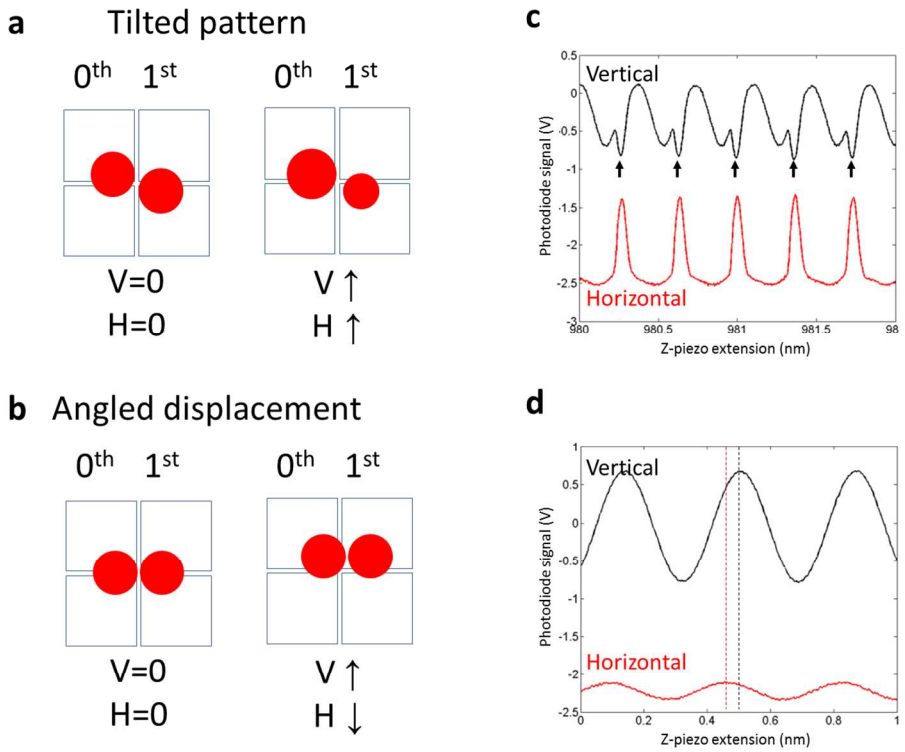

Figure S7. Vertical-horizontal signal cross-talk due to optical misalignments. a. Tilted pattern of the 0^{th} and 1^{st} order spots on the photodetector causes a response in the vertical signal to changes in force sensor signal. **b.** Angled displacement of the whole diffraction pattern causes a false force (horizontal) signal in response to changes in vertical deflection of the cantilever. **c.** An example of the presence of a force signal in the vertical deflection signal (arrows) when tapping the glass substrate. **d.** Phase difference (marked by the dotted lines) between the vertical and horizontal signals when the probe was oscillating 1 μm away from the substrate, indicating non-negligible hydrodynamic forces and vertical-to-horizontal cross-talk.

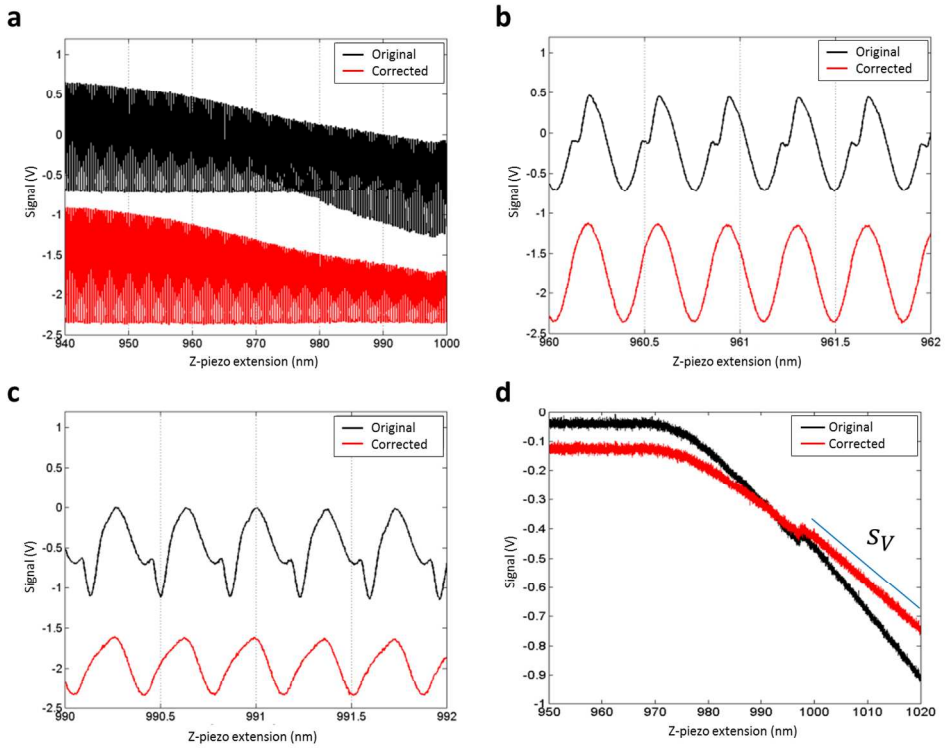

Figure S8. Cross-talk removal from the vertical signal. The top curves (black) for all panels are the original vertical signal, V_m , and the bottom curves (red) are the corrected vertical signal, V_r, calculated by removing high frequency components above the 2nd harmonic from V_m. The DC component of these curves associated with Z-piezo extension was removed for clarity. **a.** Vertical signals from the tapping mode force curve where the overall amplitude decreased with Z-piezo extension. Note the high frequency components in the original signal increased with Z-piezo extension, suggestion horizontal-to-vertical coupling. **b.** Zoom-in to a light tapping part of the force curve. The correction restored the vertical deflection close to a sinusoidal waveform. **c.** Zoom-in to a hard tapping part of the force curve. The obvious distortion of the corrected signal was due to the remaining 2nd harmonic component in the vertical signal. **d.** Vertical signals from the contact mode force curve were used to extract the vertical optical sensitivity, s_V.

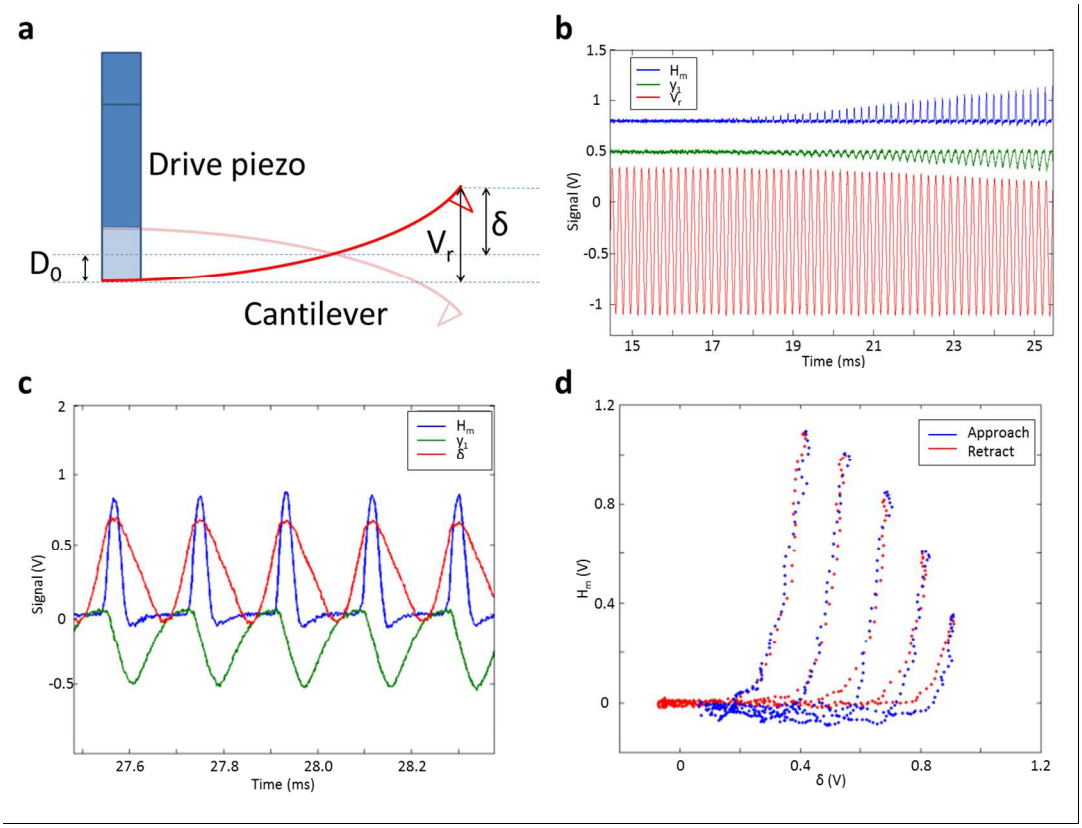

Figure S9. Calculation of tip position from a tapping mode force curve. a. Cartoon showing the large base motion when using acoustic excitation to drive a cantilever in liquid. In this case, the vertical deflection of the cantilever, V_r, is not equal to the tip position δ. **b.** Tapping mode force curve showing the horizontal signal (H_m, blue curve), cross-talk corrected vertical signal (V_r, red curve), and the calculated reduction of the vertical signal when tapping the glass substrate (y_1, green curve). **c.** Zoom-in to a hard tapping part of the force curve showing H_m(blue curve), y_1 (green curve), and the calculated tip position δ (red curve). **d.** Reconstructed force-distance curves. δ is shown in the unit of volts and was converted to nm using the optical sensitivity s_V= 65 nm/V.

Supporting Information Notes

Signals from interdigitated probes require specialized processing and analysis to obtain correct information of the nanomechanical properties. These supplementary notes contain three parts addressing the optical, mechanical, and statistical analysis and calculation of the raw AFM signal.

Correction of vertical-horizontal cross-talk and optical sensitivity calibration

In the most simplified optical setting of the interdigitated probes, the vertical signal (V_m for "measured" photodiode output) of the quadrant photodiode solely depends on the deflection of the main cantilever (V_r for "real" deflection in nanometers) and the horizontal signal (H_m) on the deflection of the interferometric force sensor (H_r, deflection of the tip-coupled fingers with respect to the reference fingers) as follows:

$$\begin{matrix} V_m = s_V V_r \\ H_m = s_H H_r \end{matrix}, \quad \text{(S1)}$$

where s_V and s_H are the optical-lever sensitivity, relating deflection in the units of distance to photodiode voltages.

In reality, the physical deflection of the cantilever and the sensor contribute to changes in both vertical and horizontal signals due to misalignment of the optics (Supporting Information Fig. 7a-b). For example, when the diffraction pattern is not horizontally aligned to the photodiode ("tilted pattern"), the changing power of the 0th and 1st order diffraction spots (due to deflection of the tip-coupled fingers) results in changes in both channels. These misalignments result in linear combinations of both cantilever and sensor deflection in the detected signals, as given by

$$\begin{matrix} V_m = AV_r + \alpha H_r \\ H_m = BH_r + \beta V_r \end{matrix}, \quad \text{(S2)}$$

where the coupling coefficients A and B generally are much greater than the cross-talk coefficients α and β.

To decouple V_m and H_m in Eq. S2 and obtain the real deflections, V_r and H_r, a calibration procedure using a contact mode force curve (CMFC) and a tapping mode force curve (TMFC) on the glass substrate in imaging liquid was performed. To minimize possible optical and mechanical artifacts, we performed *in situ* calibration on the substrate nearby each cell being imaged.

First, in the TMFC measurement, the probe was driven at the resonance frequency of the main cantilever and approached the surface at a loading rate of 1 μm/s. The tip-sample interaction force (F_{ts}) caused momentary deflection, H_r, of the high-bandwidth force sensor and reduced the vibrational amplitude of the deflection, V_r, of the body cantilever. Due to the low mechanical bandwidth of the body cantilever, we assumed that the frequency component of the deflection signal V_r above the 2nd order harmonics was attenuated and negligible, such that any higher order harmonic in V_r were due to coupling from H_r (Supporting Information Fig. 7c), e.g., for the third harmonics, $V_{r,3} \cong 0$, so that Eq. S2 was simplified to

$$\begin{matrix} V_{m,3} \cong \alpha H_{r,3} \\ H_{m,3} \cong B H_{r,3} \end{matrix} . \quad \text{(S3)}$$

A new factor κ can be defined by

$$\kappa = \frac{B}{\alpha} \cong \frac{H_{m,3}}{V_{m,3}} , \quad \text{(S4)}$$

such that the contribution from H_r can be eliminated from the measured vertical signal V_m by using

$$V_m - \kappa H_m \cong (A - \kappa\beta)V_r = s_V V_r . \quad \text{(S5)}$$

Finally, to calculate the real deflection of the cantilever, V_r, the vertical sensitivity, s_V, was determined from the CMFC (no drive and at a loading rate of 1 μm/s) where V_r was equivalent to the Z-piezo extension during the contact with the glass surface (assuming indentation into glass was negligible and all Z-piezo extension was transferred into cantilever

deflection). Supporting Information Fig. S8 shows an example of using the method above to obtain corrected deflection of the cantilever.

To decouple H_r from the mixed signals, one could measure the driven oscillation far away (>30 μm) from the surface where hydrodynamic force is weak. The so-called squeeze-film effect could introduce a non-negligible hydrodynamic force manifested as a sinusoidal undulation in H_r and result in a phase difference between V_m and H_m (Supporting Information Fig. 7d). When the probe was far away from the surface, $H_{r,far} \cong 0$, and V_m and H_m were in phase, i.e.,

$$\begin{matrix} V_{m,far} \cong AV_{r,far} \\ H_{m,far} \cong \beta V_{r,far} \end{matrix} . \quad \text{(S6)}$$

Similar to Eq. S4 and S5, we may define

$$\lambda = \frac{A}{\beta} \cong \frac{V_{m,far}}{H_{m,far}} \quad \text{(S7)}$$

and calculate

$$H_m - \lambda V_m \cong (B - \lambda\alpha)H_r = s_H H_r . \quad \text{(S8)}$$

To calibrate for the horizontal sensitivity, s_H, we extracted the real horizontal deflection, H_r, using the CMFC. Assuming the sensor and the cantilever behaved as a serially-coupled spring system, $\frac{H_r}{V_r} = \frac{k_{sens}}{k_{canti}}$, where k_{sens} and k_{canti} were the spring constants of the sensor and cantilever, respectively. The spring constants were estimated using finite element analysis based on the exact dimensions of the probe, as measured by SEM. Ideally, we need to collect signals far away from the substrate to perform this calibration. Yet most calibrations in the work were performed at a distance of ~1 μm away from the substrate, not far enough to fulfill the assumption required for Eq. S6. Hence, the horizontal signal was not treated with the method of cross-coupling removal proposed here and the horizontal sensitivity, s_H, was derived from the uncorrected $H_m$of the contact force curve (i.e., assuming $\lambda = 0$ in Eq. S8).

Calculation of tip position and indentation using TMFC

Due to viscous damping in an aqueous environment, the drive amplitude at the base of the cantilever was comparable to the deflection amplitude and hence the corrected vertical deflection of the cantilever, V_r, could not be used directly as the tip position (Supporting Information Fig. S9a). As this drive motion was generally not measured, we developed a method to estimate the drive motion (i.e., drive amplitude and phase) applied to the base of the cantilever by the drive piezo using the TMFC. We first parameterized the tip position $\delta(t)$ for the non-tapping part of the TMFC, which was the sum of the corrected vertical deflection (V_r), drive (D), and the Z-piezo extension (Z):

$$\delta(t) = V_r(t) + D(t) + Z(t) \tag{S9}$$

or

$$\delta(t) = y_0 \sin(\omega t) + D_0 sin(\omega t + \varphi) + Z(t). \tag{S10}$$

where y_0 and D_0 were the oscillation amplitude of $V_r(t)$ and $D(t)$, ω the drive frequency and φ the phase difference between $V_r(t)$ and $D(t)$. $Z(t)$ was linear at the loading rate of 1 μm/s. Obviously, without the linear part, $Z(t)$, the tip position $\delta(t)$ varied in time as a simple sinusoidal oscillation with an amplitude $A(y_0, D_0, \varphi)$ and phase $\vartheta(y_0, D_0, \varphi)$ as functions of the deflection and drive amplitudes and phase. For the tapping part of the force curve, due to the presence of F_{ts}, the deflection amplitude was suppressed as Z-piezo extended. So, we introduced the reduction in deflection amplitude ($y_1(t)$) as a second component of V_r (t). The tip position during contact was hence given by

$$\delta'(t) = [y_0 \sin(\omega t) + y_1(t)] + D sin(\omega t + \varphi) + Z(t). \tag{S11}$$

Substituting Eq. S9 and S10 into S11, gives the tip position in the tapping part of the force curve as

$$\delta'(t) - Z(t) = y_1(t) + Asin(\omega t + \vartheta) \ , \quad \text{(S12)}$$

where $n(\omega t + \vartheta) = y_0 \sin(\omega t) + Dsin(\omega t + \varphi)$. This final equation showed that the tip position during contact, $\delta'(t)$, subtracting $Z(t)$, was the sum of $y_1(t)$ and a simple sinusoidal function, $Asin(\omega t + \vartheta)$. Once the amplitude and phase of this sinusoidal function was determined, the actual drive amplitude and phase could be calculated using Eq. S10.

Supporting Information Fig. S9 shows an example of calculating tip position from a measured TMFC. To calculate y_1, the non-tapping part of the force curve was fitted to a sine function to obtain $y_0 \sin(\omega t)$. The sine function was then subtracted from the tapping part to yield y_1. We found, partly due to the low bandwidth, that the cantilever responded to the tip-sample force slowly and the change spanned across the whole oscillation cycle (y_1, Supporting Information Fig. S9b-c). Finally, to calculate the tip position, $\delta'(t)$, a sine function $Asin(\omega t + \vartheta)$ with a combination of different values of A and ϑ was added to y_1 and the force-distance curves for several randomly selected taps were reconstructed. The combination of A and ϑ yielding the most overlapped approach and retract parts of the reconstructed force curves were used to calculate the tip position and indentation for the whole image (Supporting Information Fig. S9d).

Calculation of nanomechanical properties from reconstructed force curves

The reconstructed force-distance curve contains many important nanomechanical properties and can give insights into the elastic, viscoelastic, and adhesive nature of cells at the nanoscale. We extracted elastic moduli (E^*) from both the loading and unloading part of the force curve. For loading elastic moduli (E^*_{load}), segments of loading part from different ranges of indentation (δ) were used, depending on the application (e.g., for RBCs, the first 25 nm was used and, for stiffness tomography on HeLa cells, three ranges (0-80, 80-160, and >160 nm) were used). For unloading elastic moduli (E^*_{unload}), only one segment, the higher 50% of the unloading force curve between the maximal force (peak repulsive force, F_{max}) and minimal force

(adhesion force, F_{adh}), was used. Assuming a cone-shaped tip geometry, the Hertzian contact mechanical model including adhesion force gave

$$F_{ts,load}(\delta) = \frac{2}{\pi tan\theta} E^*_{load}\delta^2, \quad \text{(S13)}$$

and

$$F_{ts,unload}(\delta) - F_{adh} = \frac{2}{\pi tan\theta} E^*_{unload}\delta^2, \quad \text{(S14)}$$

where the elastic moduli E^* here were the reduced Young's moduli and θ the half-cone angle of the tip, which was ~15°.

To calculate energy dissipation during tip-sample interactions, we integrated the hysteresis area enclosed by the loading and unloading force curves and divided the total energy into two parts: the area of $F_{ts} > 0$ for dissipation based on indentation of the sample (W_{ind}) and the area of $F_{ts} < 0$ for dissipation from the adhesion between the tip and the sample (W_{adh}) (Fig. 2d).

Weighted bootstrapping method for high resolution stiffness tomography

In conventional force-volume stiffness mapping, the local stiffness is measured only once at the same location if the closest spacing between two points in the map is greater than the size of the contact area. Hence, no statistical assessment can be performed to address the confidence in the local stiffness measurement. Here, using high-bandwidth AFM, local stiffness was measured multiple times through the tightly spaced taps (~0.3 nm), allowing us to evaluate the local stiffness measurements statistically. The standard statistic calculated for most images in this paper was the median stiffness from 25 consecutive taps in the same pixel, which correspond to an ~7 nm wide area being probed by an ~ 10 nm sized tip. Median calculations removed outliers of stiffness values and offered a statistically meaningful representation of the local stiffness. A second method using weighed bootstrapping was applied to the stiffness tomograms of HeLa cells (Fig. 3). This method required longer computation time in exchange

for robustness. This method was also motivated by the observation that many outliers had higher goodness-of-fit from the fitting of the Hertzian model, suggesting they should be weighted more into the final stiffness value in the image. In the weighted bootstrapping method, the weighting determined the probability of one particular stiffness value being sampled as follows:

$$w_i = {R^2}_i \times G_i \tag{S15}$$

where i = 1,…,25, ${R^2}_i$ was the goodness-of-fit R-square value from the fitting for tap i , and G_i was the spatial Gaussian weight which was one for the center tap (i=13) and 0.01 for the first and last tap (i.e., i =1 and 25)(Supporting Information Fig. S4c). The 25 stiffness values were then resampled 1600 times with the weightings given above. The mean, but not median, of the resamples was calculated and the empirical distribution of stiffness means from the 1600 resample means was pooled into a histogram (Supporting Information Fig. S4d). Instead of using resampled medians, we used resampled means in combination with the resampling weightings to better address the contribution of stiffness values from high goodness-of-fit force curves, whether the stiffness values were outliers or not. The empirical distribution usually did not follow a normal distribution. Therefore, we chose the median of resampled means to represent the whole distribution in the final image.